

Spatial Patterns of Atrophy, Hypometabolism, and Amyloid Deposition in Alzheimer's Disease Correspond to Dissociable Functional Brain Networks

Michel J. Grothe,^{1*} and Stefan J. Teipel,^{1,2}
for the Alzheimer's Disease Neuroimaging Initiative

¹German Center for Neurodegenerative Diseases (DZNE), Gehlsheimer Str. 20, Rostock, 18147, Germany

²Department of Psychosomatic Medicine, University of Rostock, Gehlsheimer Str. 20, Rostock, 18147, Germany



Abstract: Recent neuroimaging studies of Alzheimer's disease (AD) have emphasized topographical similarities between AD-related brain changes and a prominent cortical association network called the default-mode network (DMN). However, the specificity of distinct imaging abnormalities for the DMN compared to other intrinsic connectivity networks (ICNs) of the limbic and heteromodal association cortex has not yet been examined systematically. We assessed regional amyloid load using AV45-PET, neuronal metabolism using FDG-PET, and gray matter volume using structural MRI in 473 participants from the Alzheimer's Disease Neuroimaging Initiative, including preclinical, prodementia, and clinically manifest AD stages. Complementary region-of-interest and voxel-based analyses were used to assess disease stage- and modality-specific changes within seven principle ICNs of the human brain as defined by a standardized functional connectivity atlas. Amyloid deposition in AD dementia showed a preference for the DMN, but high effect sizes were also observed for other neocortical ICNs, most notably the frontoparietal-control network. Atrophic changes were most specific for an anterior limbic network, followed by the DMN, whereas other neocortical networks were relatively spared. Hypometabolism appeared to be a mixture of both amyloid- and atrophy-related profiles. Similar patterns of modality-dependent network specificity were also observed in the prodementia and, for amyloid deposition, in the preclinical stage. These quantitative data confirm a high vulnerability of the DMN for multimodal imaging abnormalities in AD. However, rather than being selective for the DMN, imaging abnormalities more generally affect higher order cognitive networks and, importantly, the vulnerability

Data used in preparation of this article were obtained from the Alzheimer's Disease Neuroimaging Initiative (ADNI) database (<http://adni.loni.usc.edu/>). As such, the investigators within the ADNI contributed to the design and implementation of ADNI and/or provided data but did not participate in analysis or writing of this report. A complete listing of ADNI investigators can be found at: http://adni.loni.usc.edu/wp-content/uploads/how_to_apply/ADNI_Acknowledgement_List.pdf

Contract grant sponsor: National Institutes of Health; Contract grant number: U01 AG024904; Contract grant sponsor: Department of Defense; Contract grant number: W81XWH-12-2-0012.

*Correspondence to: Michel J. Grothe, Ph.D., German Center for Neurodegenerative Diseases (DZNE), Rostock, Gehlsheimer Str. 20, 18147 Rostock, Germany. E-mail: michel.grothe@dzne.de

Received for publication 5 August 2015; Revised 18 September 2015; Accepted 23 September 2015.

DOI: 10.1002/hbm.23018

Published online 00 Month 2015 in Wiley Online Library (wileyonlinelibrary.com).

profiles of these networks markedly differ for distinct aspects of AD pathology. *Hum Brain Mapp* 00:000–000, 2015. © 2015 Wiley Periodicals, Inc.

Key words: default mode network; intrinsic connectivity networks; resting-state functional MRI; AV45-PET; FDG-PET; mild cognitive impairment; preclinical; predementia; voxel-based

INTRODUCTION

Alzheimer's disease (AD) is a neurodegenerative brain disorder that is characterized by molecular alterations in the form of amyloid plaques and neurofibrillary tangles, which are accompanied by neuronal dysfunction, degeneration, and ultimately neuronal loss. Early neuropathological studies have shown that the pathologic alterations in AD are not randomly distributed throughout the entire brain but appear to specifically affect discrete neuronal systems corresponding to limbic and heteromodal association areas of the cortex, whereas primary sensory-motor areas are relatively spared [Braak and Braak, 1991]. However, the exact nature of these neuronal systems and the shared characteristics that render them particularly vulnerable to AD pathology has remained elusive so far.

Research on the regional specificity of AD-related brain changes has been greatly facilitated by the development of neuroimaging techniques that allow imaging diverse aspects of AD pathology in the living human brain, most notably PET-based imaging of amyloid deposition and neuronal hypometabolism, as well as high-resolution MRI for the assessment of regional gray matter atrophy. In addition, recent advances in functional imaging techniques have led to new insights regarding the network-level organization of interconnected neuronal systems in the human brain. Thus, resting-state functional MRI (rs-fMRI) studies have provided substantial evidence that the human brain can be subdivided into consistent sets of functional brain networks based on their interregional coherence of spontaneous activity fluctuations during rest [Power, et al., 2011; Smith, et al., 2009; Yeo, et al., 2011]. Observations of topographical similarities between regional patterns of AD-related imaging abnormalities and a specific network called the default-mode network (DMN) have led to the

popular claim that AD pathology may specifically target this functional brain network typically involved in introspective cognition and autobiographical memory [Buckner, et al., 2005; Fjell, et al., 2013; Oh, et al., 2014; Seeley, et al., 2009; Shin, et al., 2010; Sperling, et al., 2009; Tosun, et al., 2011].

However, although AD-related imaging abnormalities within the DMN are well replicated research findings, the specificity of the pathologic changes for the DMN compared to other functional networks has received considerable less attention so far. Thus, if assessed at all, the specificity of imaging abnormalities for the DMN was typically demonstrated in comparison to alterations in sensory-motor networks, hence providing little evidence for the increased vulnerability of the DMN compared to other functional brain networks implicated in higher cognitive functions [Drzezga, et al., 2011; Royall, et al., 2012; Sala-Llonch, et al., 2010; Zhu, et al., 2013].

At least two recent observations warrant a more detailed examination of the network-specificity of AD-related neuroimaging abnormalities. First, detailed mappings of the brain's functional network structure indicate that anatomically broadly defined sites of AD-typical neurodegeneration, such as posterior cingulate/precuneus, temporoparietal associative cortex, or medial temporal lobe (MTL) [Villeneuve, et al., 2015], are not functionally homogeneous structures but cover distinct nodes of dissociable large-scale functional brain networks [Leech, et al., 2012; Mars, et al., 2012; Ranganath and Ritchey, 2012; Yeo, et al., 2011]. Second, several studies using multimodal imaging assessments of AD-related brain changes have described noticeable divergences in the regional profiles of amyloid deposition, hypometabolism, and gray matter atrophy [Edison, et al., 2007; Kljajevic, et al., 2014; La Joie, et al., 2012; Mosconi, et al., 2013], and it is not clear how these inter-modality differences relate to the network-specificity of imaging abnormalities in AD.

In the present study we used rich multimodal imaging data of a large study sample, including preclinical, predementia, and clinically-manifest AD stages, to robustly estimate AD-related patterns of amyloid deposition, hypometabolism, and gray matter atrophy, and assessed their correspondence with the principle functional networks of the human brain as defined by a standardized functional connectivity atlas based on rs-fMRI data of 1000 healthy young adults. To test the sensitivity of our findings for the a priori selection of a specific functional network parcellation, we additionally used a complementary data driven approach based on independent component analysis (ICA) of rs-fMRI data from an independent

Abbreviations

AD	Alzheimer's disease
DMN	default-mode network
FWHM	full-width at half maximum
FPN	frontoparietal-control network
GOF	goodness-of-fit
ICA	independent component analysis
ICNs	intrinsic connectivity networks
SMN	somatomotor networks
SUVr	standard uptake value ratios
TIV	total intracranial volume

sample of healthy subjects spanning the age range from adolescence to advanced age.

MATERIAL AND METHODS

Data Source

Data used in the preparation of this article were obtained from the ADNI database (adni.loni.usc.edu). The ADNI was launched in 2003 by the National Institute on Aging, the National Institute of Biomedical Imaging and Bioengineering, the Food and Drug Administration, private pharmaceutical companies and non-profit organizations, with the primary goal of testing whether neuroimaging, neuropsychologic, and other biologic measurements can be used as reliable in-vivo markers of AD pathogenesis. A fuller description of ADNI and up-to-date information is available at www.adni-info.org.

Subjects

AV45- and FDG-PET as well as structural MRI scans were retrieved from the ADNI-GO and ADNI-2 extensions of the ADNI project and included imaging data of 179 cognitively normal elderly subjects (CN), 269 subjects with early stage mild cognitive impairment (EMCI), 134 subjects in a more advanced stage of MCI (LMCI), and 85 subjects with AD dementia.

Detailed inclusion criteria for the diagnostic categories can be found at the ADNI website (<http://www.adni.loni.usc.edu/methods/>). Briefly, CN subjects have Mini Mental Status Examination (MMSE) scores between 24 and 30 (inclusive), a CDR = 0, are non-depressed, non-MCI, and non-demented. EMCI subjects have MMSE scores between 24 and 30 (inclusive), a subjective memory concern reported by subject, informant, or clinician, objective memory loss measured by education adjusted scores on delayed recall (one paragraph from Wechsler Memory Scale Logical Memory II; education adjusted scores: ≥ 16 years: 9–11; 8–15 years: 5–9; 0–7 years: 3–6), a CDR = 0.5, absence of significant levels of impairment in other cognitive domains, essentially preserved activities of daily living, and an absence of dementia. Diagnosis of LMCI differs from that of EMCI only in a higher degree of objective memory impairment (education adjusted scores: ≥ 16 years: ≤ 8 ; 8–15 years: ≤ 4 ; 0–7 years: ≤ 2). Subjects with AD dementia have initial MMSE scores between 20–26 (inclusive), a CDR = 0.5 or 1.0 and fulfill NINCDS-ADRDA criteria for clinically probable Alzheimer’s disease [McKhann, et al., 1984].

Diagnostic groups were dichotomized into amyloid-positive (+) and amyloid-negative (–) subgroups, based on AV45-PET evidence of global amyloid pathology indicative of AD. Cortex-to-whole cerebellum AV45 standard uptake value ratios (SUVR) have been calculated and made available on the ADNI server by one of the ADNI PET core

laboratories (Jagust Lab, UC Berkley). Based on these values, amyloid-positivity was established using a recommended threshold of $SUVR \geq 1.11$ [Landau, et al., 2013].

Amyloid-negative MCI and AD subjects were omitted from analyses, which resulted in a final sample size of 473 subjects: 126 CN- subjects, representing the control group, and 53 CN+, 126 EMCI+, 93 LMCI+, and 75 AD+ subjects, representing preclinical, early and late pre-dementia, and clinically manifest AD groups, respectively [Albert, et al., 2011; McKhann, et al., 2011; Sperling, et al., 2011].

Imaging Data Acquisition

ADNI-GO/-2 MRI data were acquired on multiple 3-T MRI scanners using scanner-specific T1-weighted sagittal 3D MPRAGE sequences. In order to increase signal uniformity across the multicenter scanner platforms, original MPRAGE acquisitions in ADNI undergo standardized image pre-processing correction steps. AV45- and FDG-PET data were acquired on multiple instruments of varying resolution and following different platform-specific acquisition protocols. Similar to the MRI data, PET data in ADNI undergo standardized image pre-processing correction steps aimed at increasing data uniformity across the multicenter acquisitions. More detailed information on the different imaging protocols employed across ADNI sites and standardized image pre-processing steps for MRI and PET acquisitions can be found on the ADNI website (<http://adni.loni.usc.edu/methods/>)

Imaging Data Processing

Imaging data were processed by using statistical parametric mapping (SPM8, Wellcome Trust Center for Neuroimaging) and the VBM8-toolbox (<http://dbm.neuro.uni-jena.de/vbm/>) implemented in MATLAB R2013b (MathWorks, Natick, MA) as described previously [Grothe, et al., 2014; Teipel, et al., 2014].

MRI processing

First, MRI scans were automatically segmented into gray matter (GM), white matter (WM), and cerebrospinal fluid (CSF) partitions of 1.5 mm isotropic voxel-size using the segmentation routine of the VBM8-toolbox. The resulting GM and WM partitions of each subject in native space were then high-dimensionally registered to an aging/AD-specific reference template from a previous study [Grothe, et al., 2013] using the DARTEL algorithm [Ashburner, 2007]. Individual flow-fields resulting from the DARTEL registration to the reference template were used to warp the GM segments and voxel-values were modulated for volumetric changes introduced by the high-dimensional normalization, such that the total amount of GM volume present before warping was preserved. Finally, for

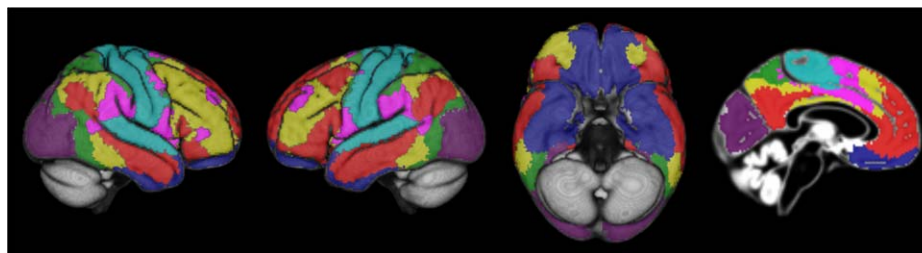


Figure 1.

Overview of the intrinsic connectivity networks. The figure shows standardized maps of seven intrinsic connectivity networks as published by Yeo et al. (2011), projected on the cortical surface and a midsagittal section of the reference template. Red: default mode network, yellow: frontoparietal-control

network, green: dorsal attention network, pink: ventral attention network, blue: limbic network, purple: visual network, cyan: somatomotor network. [Color figure can be viewed in the online issue, which is available at wileyonlinelibrary.com.]

voxel-based analyses modulated warped GM segments were smoothed with a Gaussian smoothing kernel of 8 mm full-width at half maximum (FWHM). All preprocessed GM maps passed a visual inspection for segmentation and registration accuracy.

PET data processing

Each subject's AV45- and FDG-PET scans were rigidly coregistered to a skull-stripped version of the corresponding structural MRI scan and warped (without modulation) to the aging/AD-specific reference space using the deformation fields derived from the registration of the MRI scan. Skull-stripping of the structural MRI scan was performed by multiplication with a binary mask of the combined GM and WM tissue partitions. In order to limit signal spill over from surrounding WM and CSF tissue, voxels with a GM probability of less than 50% in the aging/AD template were removed from the warped PET scans. For voxel-based analyses, preprocessed AV45- and FDG-PET scans were proportionately scaled by mean uptake values within the cerebellum and the pons, respectively, and smoothed with a Gaussian smoothing kernel of 8 mm FWHM.

Definition of Intrinsic Connectivity Networks

Definition of ICNs was based on a recently published functional parcellation scheme of the human brain into seven major functional connectivity networks, including the DMN, frontoparietal-control network (FPN), dorsal- (DAN) and ventral attention networks (VAN), limbic network (LIN), as well as visual- (VIS) and somatomotor networks (SMN) (Figure 1) [Yeo, et al., 2011] (<http://yeolab.weebly.com/software-data.html>). These reference maps represent one of the best currently available estimates of the functional connectivity architecture of the human cerebral cortex, and were generated using a clustering approach on individual whole-brain functional connectivity profiles derived from rs-fMRI data of 1000 healthy young

adults. In this approach, each cortical voxel is assigned to a single best fitting cluster, resulting in non-overlapping networks that consist of functionally interconnected brain regions and together cover the whole cortical gray matter. The so-defined networks were found to be highly reproducible across independent discovery and replication datasets, and nicely converge with previous reports of consistent large-scale functional connectivity networks derived from rs-fMRI using a wide variety of analytic methods, including seed-based functional connectivity analysis [Fox, et al., 2006; Greicius, et al., 2003; Kahn, et al., 2008; Pascual, et al., 2015; Seeley, et al., 2007; Vincent, et al., 2008; Vincent, et al., 2006], ICA [Damoiseaux, et al., 2006; Smith, et al., 2009], as well as different clustering and graph theoretical methods [Bellec, et al., 2010; Cohen, et al., 2008; Dosenbach, et al., 2007; Power, et al., 2011]. However, it has to be noted that there is currently no established way of unambiguously defining the most appropriate number of separate connectivity networks within the brain's functional connectivity architecture. Although the clustering results were found to be particularly stable for a seven network solution, other numbers of clustering solutions are also possible, resulting in fusion or further subparcellation of these seven ICNs at lower and higher parcellation resolutions, respectively [Andrews-Hanna, et al., 2010; Fox, et al., 2005; Power, et al., 2011; Shirer, et al., 2012; Yeo, et al., 2011]. The naming convention for the seven different ICNs is based on common names associated with each network in the wider neuroimaging literature [Yeo, et al., 2011]. While most of these terms are suggestive of specific cognitive functions believed to be associated with the respective network, it is important to note that ICNs were solely defined based on resting-state functional connectivity characteristics, independent of any possible association with cognition or behavior. Furthermore, alternative terms for some of these networks (or subnetworks thereof) are also found frequently in the literature, such as "central-executive" or "executive-control" network for the FPN, and "salience" or "cingulo-opercular" network for the VAN.

Data Extraction and Statistical Analysis

Data extraction and statistical analyses were carried out using SPM8 in combination with in-house written MATLAB scripts, and the software package IBM SPSS Statistics version 21, respectively. Demographic characteristics were compared between each of the amyloid-positive groups and the CN- control group using Student's *t* tests for continuous variables and Fisher's exact tests for categorical variables.

Differences between AD stages and healthy controls

ROI-based analysis. Individual mean AV45- and FDG-uptake values within each of the seven ICNs were extracted from the preprocessed PET maps by averaging the voxel values within the respective ICN template masks. AV45- and FDG-uptake means were converted to SUVRs by normalization to the mean uptake values within the cerebellum and the pons, respectively. Individual GM volumes of each of the seven ICNs were extracted from the warped GM segments by summing up the modulated GM voxel values within the respective ICN template masks. These values were scaled by the total intracranial volume (TIV), calculated as the sum of total volumes of the GM, WM and CSF partitions. Group differences in multimodal ICN values between the AD stages and the amyloid-negative control group were assessed using ANCOVA models, controlling for age, gender, and education, with pair-wise follow-up tests for differences in the estimated marginal means. Statistical significance for group differences was set at $P < 0.05$ (two-tailed), Bonferroni-corrected for the number of tested ICNs and imaging modalities ($\alpha_{\text{crit}} = 0.0024$).

Voxel-based analysis. Complementary voxel-wise analyses were conducted to study imaging abnormalities in the different AD stages across the entire brain. Significant voxel-wise increases in regional amyloid load as well as decreases in glucose metabolism and GM volume were determined using a series of separate voxel-wise two-sample *t*-tests of the preprocessed imaging data, comparing each AD stage with the CN- control group, while controlling for age, gender, and education as confounding variables. Voxel-based analyses of the GM maps were additionally controlled for TIV. All analyses were restricted to a GM mask of the reference template, thresholded at 50% GM probability, and results were assessed at a statistical threshold of $P < 0.05$, FWE-corrected at the voxel-level.

Differences in the degree of imaging abnormalities between intrinsic connectivity networks

To assess the regional distribution profiles of imaging abnormalities in the different AD stages independently of statistical thresholding of group differences, modality-specific voxel-wise "Z-score" maps for each subject in the

CN+, EMCI+, LMCI+, and AD+ groups were calculated using mean and standard deviation of the amyloid-negative control group as reference values: [Z-score = (individual value – control mean)/control standard deviation] [Chetelat, et al., 2008; Mosconi, et al., 2013]. Prior to Z-score calculation all preprocessed AV45- and FDG-PET scans were proportionately scaled by mean uptake values within the cerebellum and the pons, respectively, and preprocessed GM maps were scaled by TIV. Z-score maps for GM and FDG-PET were reversed so that positive Z-scores indicate GM atrophy and hypometabolism, respectively.

The specificity of the imaging abnormalities for any particular ICN template was quantified for each AD stage using two complementary metrics. First, individual voxel-wise Z-score values, reflecting the degree of imaging abnormality compared to the control group, were averaged within each ICN template. Group-averaged Z-scores are an effect size estimate of the deviance of the respective group from the amyloid-negative control group and are equivalent to Glass' Δ . Second, the correspondence of the spatial distribution of imaging abnormalities with each of the seven ICN templates was quantified using goodness-of-fit (GOF) analysis of the Z-score maps. For each imaging modality and diagnostic group, ICN-specific GOF-scores were calculated as the difference between the average Z-score values of voxels falling within this ICN template and the average Z-score values of cortical voxels outside the ICN template [Greicius, et al., 2004; Lehmann, et al., 2013]. Thus, for a uniform distribution of a particular imaging abnormality across the cerebral cortex one would expect GOF-scores of all ICNs to be close to zero, independent of the overall degree of imaging abnormality, whereas positive GOF-scores for a particular ICN would indicate a relative preference of the imaging abnormality to occur within this ICN.

Statistical significance of the differences in severity (Z-scores) and spatial correspondence (GOF-scores) of imaging abnormalities between the two highest ranking ICNs was assessed for each imaging modality and AD stage by using paired *t*-tests. Statistical significance was set at $p < 0.05$ (two-tailed), Bonferroni-corrected for the number of imaging modalities ($\alpha_{\text{crit}} = 0.017$).

Complementary analysis using functional network maps derived from group independent component analysis

Given the inherent ambiguity of defining separate intrinsic connectivity networks within the global connectivity architecture of the human brain and the partial dependence of the derived networks on the analytic approach [Power, et al., 2011; Smith, et al., 2009; Yeo, et al., 2011], we examined whether the main findings of our study can be replicated when using functional network maps derived from ICA of rs-fMRI data [Allen, et al., 2011].

TABLE I. Sample characteristics

	N	Age (years)	Gender (F/M)	Education (years)	MMSE
CN-	126	72.7 (SD 6.4)	61/65	16.8 (SD 2.5)	29.1 (SD 1.2)
CN+	53	76.4 (SD 6.0) ^a	30/23	16.1 (SD 2.6)	29.0 (SD 1.0)
EMCI+	126	73.5 (SD 6.8)	52/74	15.7 (SD 2.9) ^a	28.0 (SD 1.7) ^a
LMCI+	93	72.3 (SD 7.4)	43/50	16.4 (SD 2.8)	27.1 (SD 1.9) ^a
AD+	75	75.0 (SD 8.5) ^a	35/40	15.6 (SD 2.8) ^a	22.9 (SD 2.1) ^a

^aStatistically significant ($P < 0.05$) differences compared to the amyloid-negative cognitively normal control group (CN-).

N, number of participants in each diagnostic group; F/M, female/male; MMSE, Mini Mental Status Examination; SD, standard deviation; CN+, group of amyloid-positive cognitively normal subjects; EMCI+, group of amyloid-positive subjects with early mild cognitive impairment; LMCI+, group of amyloid-positive subjects with late mild cognitive impairment; AD+, group of amyloid-positive subjects with clinically-manifest Alzheimer's disease dementia.

Several studies have shown that spatial maps of known ICNs can also be retrieved as independent components (ICs) using ICA-based decompositions of rs-fMRI data [Damoiseaux, et al., 2006; Smith, et al., 2009]. Here, we used publicly available IC spatial maps derived from a 75-component group ICA analysis using rs-fMRI data of 603 healthy subjects spanning the age range from adolescence to advanced age (mean age: 23.4 ± 9.2 ; data available at: <http://mialab.mrn.org/data/index.html>). Detailed information on the sample characteristics, rs-fMRI data, and the employed group ICA approach can be found in the corresponding publication [Allen, et al., 2011]. In order to adopt the nomenclature of the standard ICN maps used for our primary analysis [Yeo, et al., 2011], we labeled all ICs based on their GOF scores with these seven ICNs [Greicius, et al., 2004; Lehmann, et al., 2013] (see also definition of GOF score above). Maximum GOF scores for each IC ranged between 0.9 and 38.5, and ICs that did not show a GOF score ≥ 10 for any of the seven principle ICNs were considered to be artifactual (29 ICs). The remaining 46 ICs were used in spatial correlation analyses with the group averaged Z-score maps of amyloid deposition, hypometabolism, and gray matter atrophy, similar to approaches used in previous studies [Buckner, et al., 2009; Fjell, et al., 2014].

RESULTS

Demographic Characteristics

As outlined in Table I, CN- control subjects were significantly younger than CN+ ($P < 0.001$) and AD+ subjects ($P = 0.04$). Gender distribution was comparable between each of the amyloid-positive groups and the CN- control group (all $P > 0.3$). Compared to CN-, years of education were significantly less in AD+ ($P = 0.002$) and EMCI+ subjects ($P = 0.001$), but did not differ significantly in LMCI+ ($P = 0.27$) and CN+ ($P = 0.09$). As expected, EMCI+, LMCI+, and AD+ groups had significantly lower MMSE scores compared to the CN- group (all $P < 0.001$),

but MMSE scores of CN+ subjects were comparable to the control group ($P = 0.66$).

Network-Specificity of Amyloid Deposition across AD Stages

As expected by the group definition being based on global amyloid pathology, increased amyloid load compared to the control group was significant for all ICNs and throughout the entire brain in voxel-wise analyses for all AD stages (effects not shown). However, regional differences in the degree of amyloid deposition were evident in the group-averaged Z-score maps (Figure 2). Amyloid deposition was equally pronounced across wide parts of the cerebral cortex and appeared to be similarly distributed across the different AD stages. Regions of highest amyloid load corresponded to heteromodal association areas of the frontal, parietal, and lateral temporal lobes, whereas the MTL, pre- and postcentral gyri, and the occipital lobe showed the lowest amount of amyloid deposition. Averaged Z-score values for amyloid deposition were highest in the DMN and FPN, intermediate in DAN and VAN, and lowest in LIN, VIS and SMN (Figure 3). The difference in Z-score values for amyloid deposition between the DMN and FPN was significant in the AD+ ($P < 0.001$) and LMCI+ groups ($P < 0.001$), but not in the EMCI+ ($P = 0.09$) and CN+ groups ($P = 0.67$). Similarly, GOF analyses across AD stages revealed that the regional distribution profile of amyloid deposition showed the highest spatial correspondence with the DMN template, followed by the FPN template (Figure 4). The difference in GOF-scores for the DMN compared to the FPN was significant in all AD stages ($P < 0.001$) with exception of the CN+ group ($P = 0.23$).

Network-Specificity of Hypometabolism across AD Stages

Regions of significant hypometabolism across the AD stages and the corresponding Z-score maps of regional distribution profiles are depicted in Figure 5. In the AD+

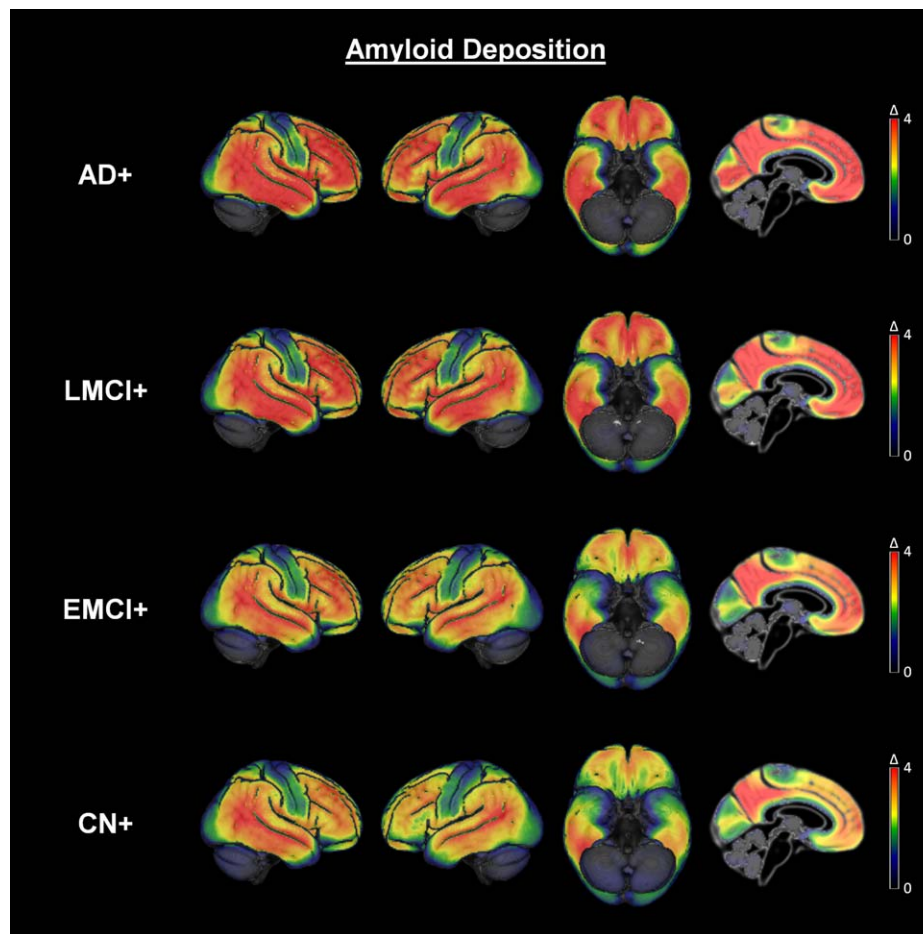


Figure 2.

Voxel-wise patterns of amyloid deposition across AD stages. Averaged voxel-wise Z-score maps of amyloid deposition as evidenced by AV45-PET in groups of clinically-manifest (AD+), predementia (LMCI+ and EMCI+), and preclinical (CN+) Alzheimer's disease are projected on the cortical surface and a midsagittal section of the reference template. Note that

these averaged Z-scores are equivalent to Glass' Δ measure of effect size and should not be confused with values of a Z statistic. Voxel-wise effects are color-coded from black/blue to yellow/red with an identical range of Glass' Δ values (0–4) for all diagnostic groups. [Color figure can be viewed in the online issue, which is available at wileyonlinelibrary.com.]

group, voxel-wise analysis revealed significant hypometabolism across wide parts of the limbic and heteromodal association cortex, showing considerable overlap with all ICNs except the VIS and SMN. In the ROI-based analysis, hypometabolism in the AD+ group was significant for all ICNs ($P < 0.001$), and the degree of hypometabolism across ICNs showed a similar distribution as for amyloid deposition, with the exception of a relatively more pronounced involvement of the LIN (Figure 3). Again, hypometabolism was significantly more pronounced in the DMN compared with the FPN ($P = 0.002$). Furthermore, the highest GOF-score of the hypometabolic pattern was obtained for the DMN, and this was significantly higher compared to the FPN ($P < 0.001$) (Figure 4).

In the LMCI+ group, significant hypometabolism occurred in very similar regions as in the AD+ group, albeit spatially more restricted, particularly within the lateral frontal lobe (Figure 5). In the ROI-based analysis, all ICNs ($P < 0.001$) with the exception of the SMN ($P = 0.003$) showed significant hypometabolism. Averaged Z-scores and GOF-scores for the ICNs showed an identical network-specific pattern of hypometabolic abnormalities as in the AD+ group (Figures 3 and 4), with a statistically significant preference for the DMN compared to the FPN, both in terms of mean Z-score ($P = 0.001$) and GOF score ($P < 0.001$).

Significant voxel-wise hypometabolism in the EMCI+ group was mainly restricted to circumscribed lateral

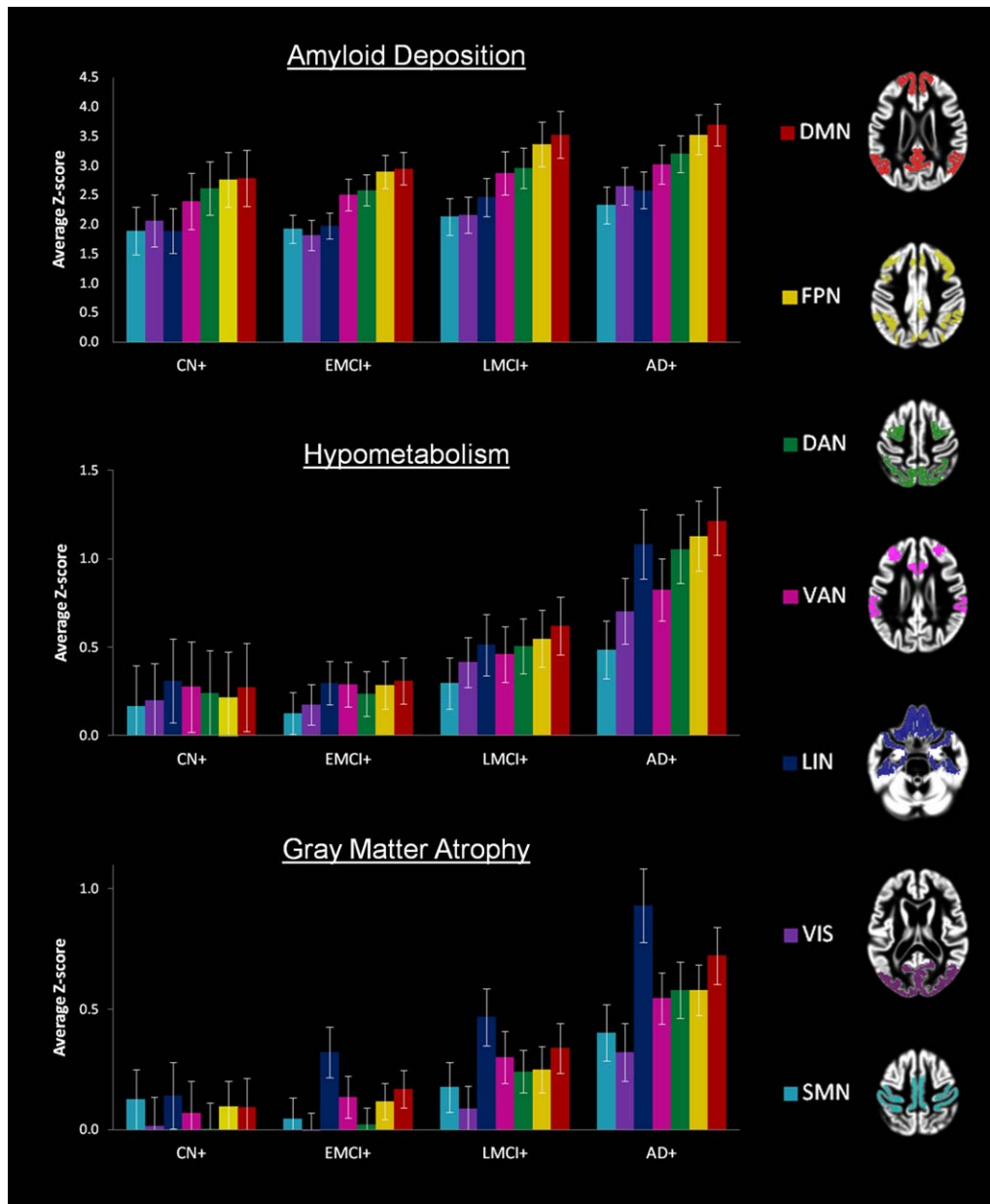


Figure 3.

Severity of AD-related imaging abnormalities within intrinsic connectivity networks. Plots depict means and 95% confidence intervals of averaged Z-scores (corresponding to Glass' Δ) of amyloid deposition (top), hypometabolism (middle), and gray matter atrophy (bottom) within the distinct intrinsic connectivity networks for each AD stage. The network-specificity of each imaging modality is largely preserved across disease stages, but differs markedly between the different imaging modalities. Note that the y-axes have been scaled to the maximum observed value for each imaging modality, and thus

bar plots represent different effect sizes across modalities. Considerably higher effect sizes for amyloid compared with GM atrophy and hypometabolism are attributable to the group definitions based on presence/absence of global amyloid pathology. Red: default mode network (DMN), yellow: frontoparietal-control network (FPN), green: dorsal attention network (DAN), pink: ventral attention network (VAN), blue: limbic network (LIN), purple: visual network (VIS), cyan: somatomotor network (SMN). [Color figure can be viewed in the online issue, which is available at wileyonlinelibrary.com.]

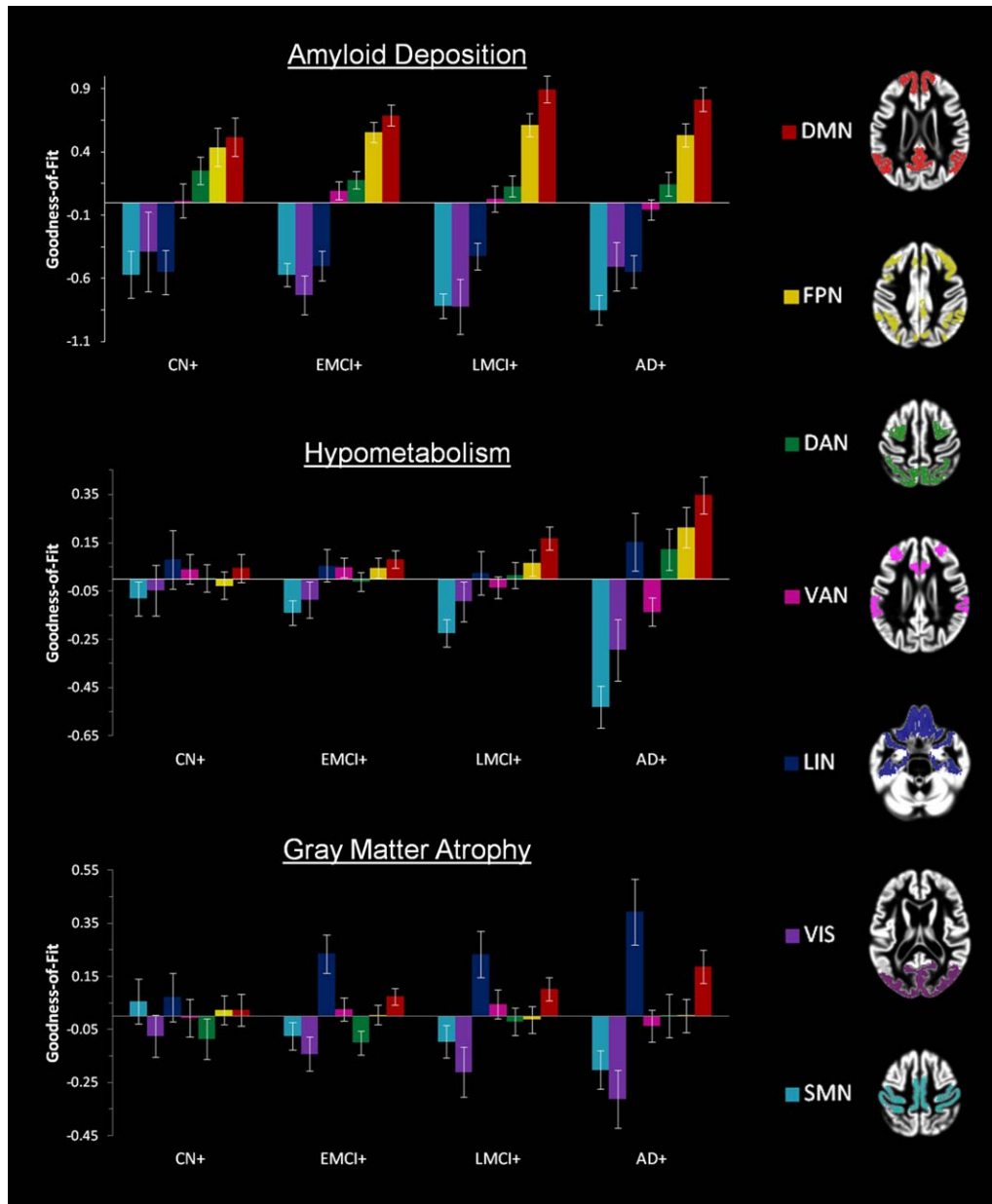


Figure 4.

Spatial correspondence between voxel-wise AD-related imaging abnormalities and intrinsic connectivity networks. Plots depict the spatial correspondence of group-specific voxel-wise pattern of amyloid deposition (top), hypometabolism (middle), and gray matter atrophy (bottom) with each of the intrinsic connectivity networks as quantified by a goodness-of-fit index. Black bars denote 95% confidence intervals. Note that similar to the plots of effect sizes (Figure 3), the preference of each imaging modality to occur within par-

temporoparietal areas, although smaller clusters were also observed in the medial and lateral frontal lobe and the left medial temporal lobe (Figure 5). In the ROI-based analysis, ticular networks is largely preserved across disease stages, but differs markedly between the different imaging modalities. Red: default mode network (DMN), yellow: frontoparietal-control network (FPN), green: dorsal attention network (DAN), pink: ventral attention network (VAN), blue: limbic network (LIN), purple: visual network (VIS), cyan: somatomotor network (SMN). [Color figure can be viewed in the online issue, which is available at wileyonlinelibrary.com.]

temporoparietal areas, although smaller clusters were also observed in the medial and lateral frontal lobe and the left medial temporal lobe (Figure 5). In the ROI-based analysis,

hypometabolism in none of the ICNs met the corrected level of statistical significance ($\alpha_{crit} = 0.0024$), but in accordance with the voxel-wise results there were trends for the

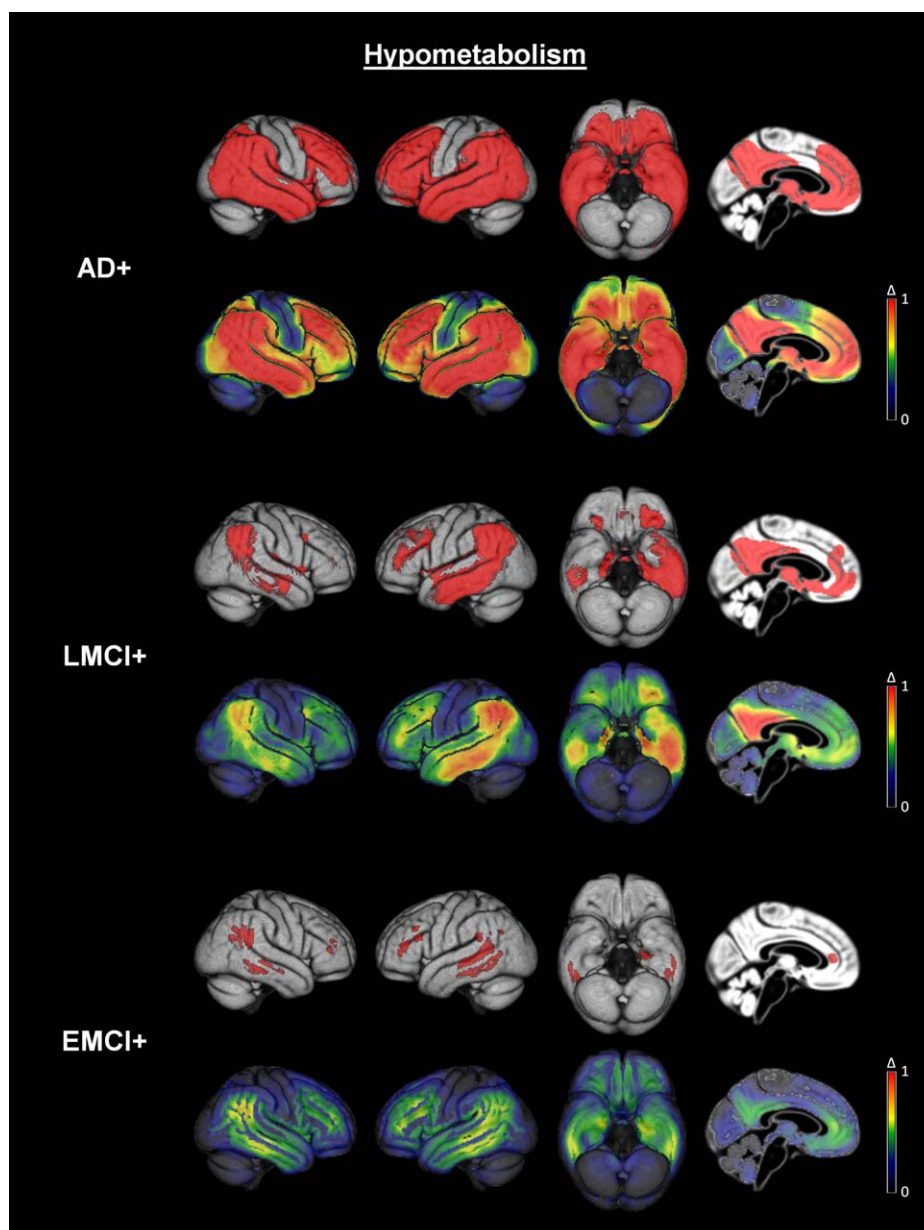


Figure 5.

Voxel-wise patterns of hypometabolism across AD stages. Voxel-wise patterns of hypometabolism compared to the healthy control group as evidenced by FDG-PET are depicted for groups of clinically-manifest (AD+), predementia (LMCI+ and EMCI+), and preclinical (CN+) Alzheimer's disease in the form of binary thresholded statistical maps (upper rows) as well as color-coded effect size maps (Glass' Δ) (lower rows). Statistical maps are corrected for age, gender,

and education, and are thresholded at $P < 0.05$, FWE-corrected at the voxel-level. Note that the intensity range for color-coding of effect size maps is identical for all diagnostic groups (Glass' Δ between 0 and 1), but differs from the range used for color-coding of effect size maps of amyloid deposition (Figure 2). [Color figure can be viewed in the online issue, which is available at wileyonlinelibrary.com.]

DMN ($P = 0.006$) and the LIN ($P = 0.007$). However, averaged Z-scores did not differ significantly between the DMN, LIN, and FPN (all $P > 0.1$). Similarly, GOF-scores of these

networks were generally very low and did not differ among each other, indicating little specificity of the hypometabolic distribution profile for any of these three networks.

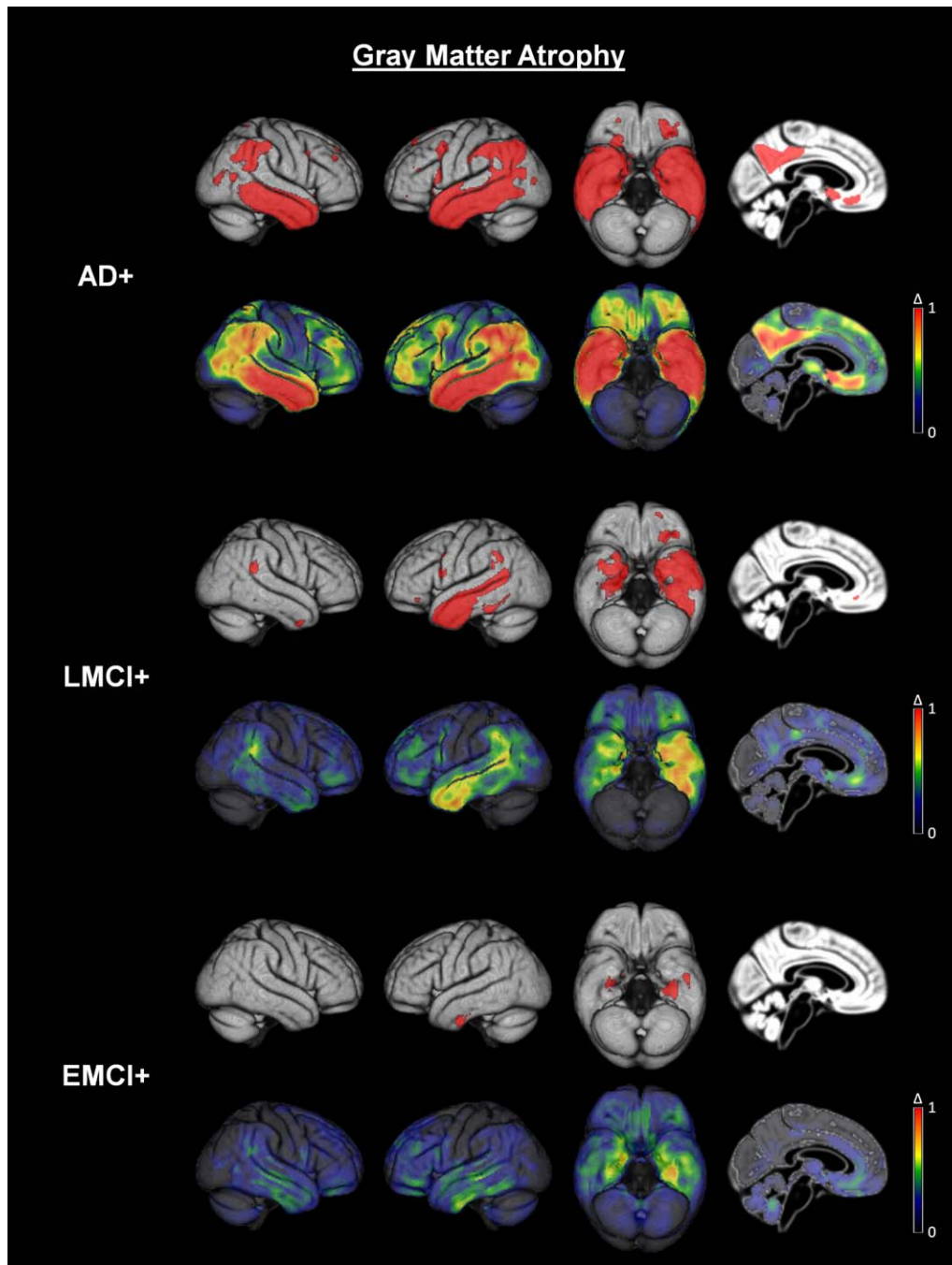


Figure 6.

Voxel-wise patterns of gray matter atrophy across AD stages. Voxel-wise patterns of gray matter atrophy compared to the healthy control group as evidenced by structural MRI are depicted for groups of clinically-manifest (AD+), pre-dementia (LMCI+ and EMCI+), and preclinical (CN+) Alzheimer's disease in the form of binary thresholded statistical maps (upper rows) as well as color-coded effect size maps (Glass' Δ) (lower rows). Statistical maps are corrected for

age, gender, and education, and are thresholded at $P < 0.05$, FWE-corrected at the voxel-level. Note that the intensity range for color-coding of effect size maps is identical for all diagnostic groups (Glass' Δ between 0 and 1), but differs from the range used for color-coding of effect size maps of amyloid deposition (Figure 2). [Color figure can be viewed in the online issue, which is available at wileyonlinelibrary.com.]

The CN+ group showed no significant effects of regional hypometabolism in either voxel-wise or ROI-based analyses, and both averaged Z-scores and GOF-scores were close to zero.

No significant ROI-wise or voxel-wise increases in glucose metabolism were present in any of the AD stages (CN+, EMCI+, LMCI+, AD+) compared to the amyloid-negative healthy reference group.

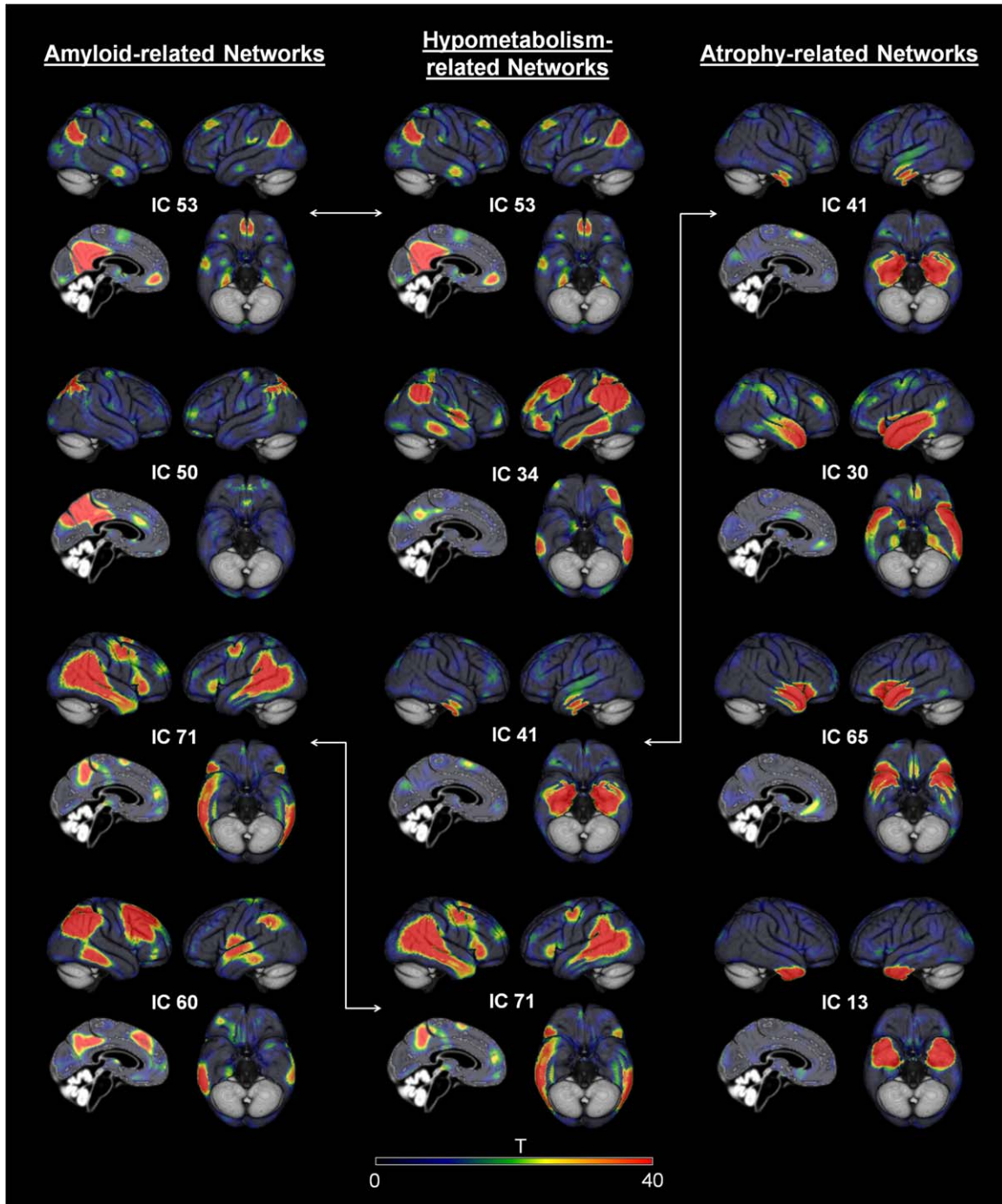


Figure 7.

Network-Specificity of Gray Matter Atrophy across AD Stages

The pattern of GM atrophy across AD stages was markedly different from the pattern of amyloid deposition (Figure 6). In the AD+ group, atrophy was most pronounced in the MTL, but significant effects were also seen in lateral temporoparietal areas, as well as anterior and posterior parts of the cingulate cortex. In contrast to both amyloid deposition and hypometabolism, large parts of the lateral and medial frontal lobes appeared to be relatively spared. GM atrophy in the AD+ group was significant for all ICNs ($P < 0.001$), but the relative pattern of atrophy severity across ICNs was strikingly different to amyloid deposition and hypometabolism: Atrophy was most pronounced in the LIN, followed by the DMN, whereas the FPN was relatively less affected (Figure 3). However, similar to the pattern of amyloid deposition and hypometabolism, the VIS and SMN were the least affected networks. Voxel-wise pattern of atrophy in the LMCI+ group were similar to the pattern in the AD+ group, but with less involvement of the cingulate cortex and lateral temporoparietal areas. In ROI-based analysis, all ICNs with the exception of the VIS ($P = 0.12$) and SMN ($P = 0.021$) showed significant atrophy compared to the CN- control group at $P < 0.001$, and the pattern of atrophy severity across the ICNs was identical to the AD+ group. In the EMCI+ group significant voxel-wise atrophy was limited to the MTL, and in the ROI-based analysis only the LIN ($P < 0.001$) showed significant atrophy compared to the CN- control group.

Across EMCI+, LMCI+, and AD+ groups, positive GOF-scores were only observed for the LIN and DMN, and within each group both averaged Z-scores and GOF-scores were significantly higher for the LIN compared to the DMN ($P < 0.002$ and $P < 0.006$ for averaged Z-scores and GOF-scores, respectively) (Figures 3 and 4).

The CN+ group showed no significant effects of regional atrophy in either voxel-wise or ROI-based analyses, and both averaged Z-scores and GOF-scores were close to zero.

No significant ROI-wise or voxel-wise increases in gray matter volume were present in any of the AD stages

(CN+, EMCI+, LMCI+, AD+) compared to the amyloid-negative healthy reference group.

Spatial Correlation Analysis with ICA-Derived Functional Network Maps

Main results of the complementary spatial correlation analysis are summarized in Table II, showing for each imaging modality the five best and the five least correlated ICs with the respective pathologic pattern in the AD dementia group (AD+). Figure 7 illustrates the spatial maps of the top four correlated ICs for each pathologic pattern. Amyloid deposition was most correlated with a component resembling the DMN (IC 53), but also showed association with other ICs corresponding to heteromodal association networks, such as the DAN and FPN. Overall, spatial correlation coefficients were rather weak ($r_{\max} = 0.26$), indicating that the regional pattern of amyloid deposition is not accurately reflected by any single IC map. The pattern of hypometabolism correlated with similar ICs as the pattern of amyloid deposition, showing highest correlation with the same DMN-associated component as amyloid deposition (IC 53). However, in contrast to the amyloid pattern, hypometabolism showed also positive correlation with a component representing a limbic network centered on the medial and inferior temporal lobe (IC 41). This same component showed highest correlation with the pattern of gray matter atrophy, and additional atrophy-correlated components represented further limbic (sub)networks involving lateral, medial, and polar temporal regions with variable contributions from the orbitofrontal cortex.

Least correlated ICs of the hypometabolic and atrophic patterns mainly corresponded to the primary sensory-motor systems (VIS and SMN), whereas the amyloid pattern also showed particularly low correlation with limbic network-associated ICs, including those that showed highest positive correlation with the atrophic and hypometabolic patterns (IC 41).

Amyloid deposition patterns in the CN+, EMCI+, and LMCI+ groups, as well as atrophic and hypometabolic patterns in the EMCI+ and LMCI+ groups, showed

Figure 7.

ICA-derived functional network maps that show highest correspondence with spatial patterns of AD-related imaging abnormalities. Figure shows selected functional network maps (independent components [IC]) derived from a high-dimensional group independent component analysis (ICA) of resting-state fMRI data from healthy individuals (Allen, et al., 2011). Depicted networks were selected based on their spatial correlation with regional patterns of amyloid deposition (IC 53, IC 50, IC 71, IC 60), hypometabolism (IC 53, IC 34, IC 41, IC 71), or gray matter atrophy (IC 41, IC 30, IC 65, IC 13) in AD dementia (see Table II). Spatial patterns of amyloid deposition and gray matter

atrophy correspond to distinct functional network maps, whereas the pattern of hypometabolism correlates with both amyloid- and atrophy-related components. ICs related to the pattern of amyloid deposition resemble large-scale heteromodal association networks spanning the frontal, temporal, and parietal neocortex, most notably the DMN (IC 53). ICs related to the pattern of gray matter atrophy resemble limbic networks centered on the medial temporal and temporopolar allocortex. Group IC maps are color-coded from $T = 0$ (black) to $T = 40$ (red). [Color figure can be viewed in the online issue, which is available at wileyonlinelibrary.com.]

TABLE II. Spatial correlations between patterns of Alzheimer’s disease-related imaging abnormalities and ICA-derived functional network maps

Amyloid			Hypometabolism			Gray Matter Atrophy		
#IC	R	ICN(Yeo)	#IC	R	ICN(Yeo)	#IC	R	ICN(Yeo)
53	0.26	DMN	53	0.30	DMN	41	0.45	LIN
50	0.22	DAN	34	0.30	DMN/FPN	30	0.24	DMN/LIN
71	0.18	DMN/VAN	41	0.28	LIN	65	0.24	LIN/DMN
60	0.16	FPN	71	0.19	DMN/VAN	13	0.22	LIN
68	0.16	FPN	50	0.18	DAN	35	0.15	LIN
41	-0.19	LIN	46	-0.24	VIS	64	-0.21	VIS
21	-0.13	VAN	29	-0.24	SMN	46	-0.20	VIS
23	-0.10	SMN/DAN	56	-0.23	VAN/SMN	75	-0.19	VIS
7	-0.10	SMN	7	-0.21	SMN/DAN	55	-0.13	VAN/FPN
19	-0.09	LIN	23	-0.17	SMN	59	-0.13	VIS

Rows 1–5 show the independent components that demonstrated highest spatial correlation with the respective pathologic pattern. Rows 6–10 show the independent components that were least correlated with the respective pathologic pattern. #IC: number of the independent component; R: (Pearson) spatial correlation coefficient; ICN(Yeo): intrinsic connectivity network as defined by Yeo et al. [2011] that shows the highest Goodness-of-fit for the respective IC. Note that some ICs did not clearly correspond to one particular ICN (i.e. showed positive GOF scores for more than one ICN). In these cases the ICN with the second highest GOF score is also listed.

highest spatial correlation with the same components as in the AD+ group (IC 53 for amyloid and hypometabolic pattern, IC 41 for atrophic pattern).

DISCUSSION

Understanding the heterogeneous distribution of pathologic alterations in AD and the precise nature of those neuronal systems that are more vulnerable to certain aspects of AD pathology than others is critical for a deeper understanding of AD pathogenesis. Based on visual judgments of thresholded voxel-wise maps of regional amyloid deposition, hypometabolism, or atrophy in AD, several previous imaging studies have emphasized the spatial correspondence between these imaging abnormalities and the DMN [Buckner, et al., 2005; Shin, et al., 2010; Sperling, et al., 2009]. However, this correspondence has not yet been formally quantified, and recent multimodal imaging studies also point to considerable divergences between the voxel-wise patterns of AD-related amyloid deposition, hypometabolism, and atrophy [La Joie, et al., 2012; Mosconi, et al., 2013].

The overall voxel-wise patterns of multimodal imaging abnormalities found in the present study were highly consistent with previous multimodal imaging assessments in subjects with AD dementia or MCI [Edison, et al., 2007; La Joie, et al., 2012; Mosconi, et al., 2013; Shin, et al., 2010], typically involving considerably smaller sample sizes. Here, we used recently published standardized network definitions and quantitative methods to systematically assess the correspondence of these imaging abnormalities with functional networks in the human brain. Corroborating the qualitative observations from previous studies

[Buckner, et al., 2005; Shin, et al., 2010; Sperling, et al., 2009], the DMN was confirmed to be the most affected brain network by amyloid deposition. However, high vulnerability was also noted for other heteromodal association networks, particularly the FPN, and the brain-wide regional profile of amyloid deposition could not be sufficiently described by the pattern of the DMN alone. By contrast, atrophic changes in AD were found to be most pronounced in an anterior MTL-centered limbic network, followed by the DMN, whereas other neocortical association networks, such as the FPN, were relatively spared from atrophic abnormalities. Of note, the highly atrophic limbic network was found to be among the least affected by amyloid deposition. Hypometabolism appeared to be a mixture of both amyloid- and atrophy-related profiles, showing high vulnerability for neocortical association networks, most notably the DMN, but also for the atrophic limbic network. Similar patterns of modality-dependent network specificity were also observed in the predementia and, for amyloid deposition, in the preclinical stage. Notably, these findings of a differential network-specificity of the distinct pathologic markers in AD were robust against the particular definition of the functional network maps, as identical patterns were also found when using spatial maps of functional networks derived from a different sample and using an ICA-based approach.

The limbic network found to correspond most closely to the AD-related atrophy pattern in this study resembles a previously described anterior MTL network that differs from a DMN-associated posterior MTL network in its neuronal connectivity pattern and the specific memory processes it subserves [Ranganath and Ritchey, 2012]. This network, encompassing bilateral regions of the anterior MTL, the temporal poles, and orbitofrontal regions, can be

reliably reproduced by functional connectivity analysis anchored in perirhinal/anterior entorhinal cortex seeds [Das, et al., 2015; Fan, et al., 2014; Pascual, et al., 2015], and similar spatial maps have also been reported from previous ICA-based rs-fMRI studies [Gour, et al., 2011; Jones, et al., 2012]. However, it has to be noted that temporobasal and orbitofrontal regions are particularly prone to susceptibility artifacts (signal loss and spatial distortions) in rs-fMRI acquisitions, creating uncertainty about the neuronal origin of the observed signals [Yeo, et al., 2011]. Thus, ICA components showing high spatial overlap with these regions are often attributed to artifactual sources rather than functional brain networks [Allen, et al., 2011]. While the existence of such a neuronal network is also supported by axonal tracing studies in non-human primates [Price, 2007; Ranganath and Ritchey, 2012], the true nature of the limbic ICN map and the corresponding ICs in our study cannot finally be resolved and the respective network boundaries should be interpreted with this caveat in mind.

Overall, our findings demonstrate that AD pathology does not exclusively target the DMN. Several other functional networks of the limbic and heteromodal association cortex are also significantly affected, and the relative degree to which a particular network is affected strongly depends on the type of pathologic marker. In line with previous voxel-wise analyses [La Joie, et al., 2012], these inter-modality differences in network-specificity are particularly striking between amyloid deposition and gray matter atrophy, showing a remarkable double dissociation in the limbic (high atrophy, low amyloid load) and frontoparietal-control networks (high amyloid load, low atrophy).

Network-specific alterations in AD have also been extensively studied by means of functional connectivity disruptions as assessed by rs-fMRI. While hypothesis-driven examinations of the DMN have shown consistent connectivity disruptions of this network in AD [Greicius, et al., 2004; Koch, et al., 2012; Sheline, et al., 2010], more unbiased analyses of functional connectivity alterations throughout the whole brain revealed functional connectivity disruptions also within several other ICNs, some of which showed similar effect sizes even in predementia and mild AD stages [Brier, et al., 2012; Myers, et al., 2014; Sorg, et al., 2007]. Interestingly, AD-related connectivity alterations have also been observed in the form of abnormally increased functional connectivity, particularly within medial temporal and frontal (sub)networks, which may be related to functional isolation and decoupling of these systems from regulating inputs within their wider network [Damoiseaux, et al., 2012; Pasquini, et al., 2015; Salami, et al., 2014]. While the hyperconnectivity within medial temporal networks and anterior DMN components appears to be an early, possibly compensatory, phenomenon that wanes as the disease progresses [Damoiseaux, et al., 2012; Gour, et al., 2011], increased connectivity within components of the salience/ventral attention and

frontoparietal networks has also been observed at more advanced clinical AD stages [Gour, et al., 2014; Zhou, et al., 2010].

Here we can only speculate about the underlying mechanisms that render some neuronal systems more vulnerable to certain forms of AD pathology than others. For amyloid deposition a “nodal stress” hypothesis has been posited, stating that highly connected regions in the brain (so called hubs) may be particularly vulnerable to amyloid deposition because of their increased synaptic activity [Buckner, et al., 2009; Jagust and Mormino, 2011; Myers, et al., 2014]. Thus, the degree to which a given functional network is affected by amyloid deposition may depend on its large-scale inter-connectedness within the brain, which indeed appears to be lowest in primary sensory-motor areas, intermediate in multimodal integration networks such as the VAN and DAN, and highest in the FPN and DMN [Buckner, et al., 2009; Sepulcre, et al., 2012].

Recent studies indicate that similar to amyloid deposition, AD-related atrophy pattern are spatially correlated with a region’s total connectivity in the healthy brain [Crossley, et al., 2014]. However, the strikingly different pattern of atrophic changes compared with amyloid deposition strongly suggests that both types of AD pathology are governed by at least partly diverging mechanisms. The MRI-based pattern of atrophic changes in the course of AD appears to be closely related to the regional profile of neurofibrillary tangle formation as revealed by neuropathological examinations [Vemuri, et al., 2008; Whitwell, et al., 2007], which clearly differs from neuropathological estimates of regional progression of amyloid pathology [Braak and Braak, 1991]. Zhou and colleagues tested the potential of various properties of the human brain’s functional connectome for predicting regional atrophy pattern in AD [Zhou, et al., 2012]. The authors concluded that the pattern may be best explained by a model of transneuronal spread from a disease-specific seed region to interconnected network nodes, although other factors, such as a region’s brain-wide connectivity may independently contribute to vulnerability. Interestingly, a prion-like neuron-to-neuron transmission of tau pathology has been described in transgenic animal models, where the regional spread of pathology followed the pattern of synaptic connectivity rather than spatial proximity [Ahmed, et al., 2014].

With the striking exception of the MTL, hypometabolism appeared to occur within regions of highest amyloid deposition, and the progression of hypometabolism across cross-sectionally modeled disease stages suggests a spreading among regions most affected by amyloid deposition. A similar association between the temporospatial progression patterns of hypometabolism and amyloid deposition has also been suggested based on observations in longitudinal multitracer PET data of AD dementia patients [Forster, et al., 2012]. Regional hypometabolism as

measured by FDG-PET is believed to reflect synaptic dysfunction in AD, which may be influenced by both the local toxic effects of amyloid pathology and tangle-related neurodegeneration [Spires-Jones and Hyman, 2014]. This may possibly explain the mixed regional pattern of hypometabolism, with significant effects in widespread neocortical networks characterized by high amyloid deposition as well as in the amyloid-spared but highly atrophic anterior limbic network. However, it has to be noted that the FDG-PET signal in the highly atrophic MTL regions may also be influenced by increased partial volume effects in these areas. Thus, estimates of regional FDG-PET uptake may be artificially decreased in atrophic brain regions, due to a higher contamination of the true gray matter signal with the low signal of surrounding WM and CSF tissue. Although the use of high-dimensional image normalization and restriction of the measurement to areas of high gray matter probability should theoretically reduce such effects, we did not apply a formal correction of partial volume effects in this study, and thus the pattern of regional hypometabolism should be interpreted with this possible confounder in mind. Of note, the voxel-based findings in our study are highly consistent with those of previous FDG-PET studies of AD and MCI that did use explicit partial volume correction, equally demonstrating most pronounced hypometabolism in the posterior cingulate cortex and less pronounced, but significant, hypometabolism in the medial temporal lobe [Chetelat, et al., 2008; La Joie, et al., 2012; Mevel, et al., 2007; Mosconi, et al., 2013]. Given the overlapping pattern of amyloid deposition and gray matter atrophy in the posterior cingulate cortex, an intriguing hypothesis is that the particularly high vulnerability of this region for hypometabolism may be based on the regional convergence of amyloid and neurofibrillary tangle pathology. However, in addition to local effects, regional metabolism may also be affected by lesions in remote but structurally and functionally connected areas [Chetelat, et al., 2009; Glodzik, et al., 2014; Grothe, et al., 2015]. More work needs to be done to fully characterize the pathologic mechanisms underlying the complex spatial distribution and progression pattern of neuronal hypometabolism in AD.

In summary, using quantitative methods and large multimodal imaging datasets to robustly estimate AD-related imaging abnormalities as well as functional network maps in the human brain, we confirm a high vulnerability of the DMN for AD-related imaging abnormalities. However, rather than being selective for the DMN, AD pathology appears to affect limbic and heteromodal association networks of the brain in a more general manner, and, importantly, the specific vulnerability profiles of these networks markedly differ for distinct types of pathologic markers. Future studies aiming to characterize neuronal networks that are particularly vulnerable to AD should take differences in the regional vulnerability for distinct types of pathologic markers into account.

ACKNOWLEDGMENTS

The authors have no conflicts of interests to declare. The ADNI was launched in 2003 by the National Institute on Aging (NIA), the National Institute of Biomedical Imaging and Bioengineering (NIBIB), the Food and Drug Administration (FDA), private pharmaceutical companies and non-profit organizations, as a \$60 million, 5-year public-private partnership. ADNI is funded by the National Institute on Aging, the National Institute of Biomedical Imaging and Bioengineering, and through generous contributions from the following: Alzheimer's Association; Alzheimer's Drug Discovery Foundation; Araclon Biotech; BioClinica, Inc.; Biogen Idec Inc.; Bristol-Myers Squibb Company; Eisai Inc.; Elan Pharmaceuticals, Inc.; Eli Lilly and Company; EuroImmun; F. Hoffmann-La Roche Ltd and its affiliated company Genentech, Inc.; Fujirebio; GE Healthcare; IXICO Ltd.; Janssen Alzheimer Immunotherapy Research & Development, LLC.; Johnson & Johnson Pharmaceutical Research & Development LLC.; Medpace, Inc.; Merck & Co., Inc.; Meso Scale Diagnostics, LLC.; NeuroRx Research; Neurotrack Technologies; Novartis Pharmaceuticals Corporation; Pfizer Inc.; Piramal Imaging; Servier; Synarc Inc.; and Takeda Pharmaceutical Company. The Canadian Institutes of Health Research is providing funds to support ADNI clinical sites in Canada. Private sector contributions are facilitated by the Foundation for the National Institutes of Health (www.fnih.org). The grantee organization is the Northern California Institute for Research and Education, and the study is coordinated by the Alzheimer's Disease Cooperative Study at the University of California, San Diego. ADNI data are disseminated by the Laboratory for Neuro Imaging at the University of Southern California. We would like to thank the ADNI (<http://adni.loni.usc.edu/>) and MIALAB (<http://mialab.mrn.org/index.html>) investigators for publicly sharing their valuable neuroimaging data. Parts of the presented data have been published previously as abstracts at the annual meeting of the Organization for Human Brain Mapping (OHBM), June 08-12, 2014 in Hamburg, Germany, and the Alzheimer's Association International Conference (AAIC), July 12-17, 2014 in Copenhagen, Denmark.

REFERENCES

- Ahmed Z, Cooper J, Murray TK, Garn K, McNaughton E, Clarke H, Parhizkar S, Ward MA, Cavallini A, Jackson S, Bose S, Clavaguera F, Tolnay M, Lavenir I, Goedert M, Hutton ML, O'Neill MJ (2014): A novel in vivo model of tau propagation with rapid and progressive neurofibrillary tangle pathology: the pattern of spread is determined by connectivity, not proximity. *Acta Neuropathol* 127:667–683.
- Albert MS, DeKosky ST, Dickson D, Dubois B, Feldman HH, Fox NC, Gamst A, Holtzman DM, Jagust WJ, Petersen RC, Snyder PJ, Carrillo MC, Thies B, Phelps CH (2011): The diagnosis of mild cognitive impairment due to Alzheimer's disease: recommendations from the National Institute on Aging-Alzheimer's

- Association workgroups on diagnostic guidelines for Alzheimer's disease. *Alzheimers Dement* 7:270–279.
- Allen EA, Erhardt EB, Damaraju E, Gruner W, Segall JM, Silva RF, Havlicek M, Rachakonda S, Fries J, Kalyanam R, Michael AM, Caprihan A, Turner JA, Eichele T, Adelsheim S, Bryan AD, Bustillo J, Clark VP, Feldstein Ewing SW, Filbey F, Ford CC, Hutchison K, Jung RE, Kiehl KA, Kodituwakku P, Komesu YM, Mayer AR, Pearlson GD, Phillips JP, Sadek JR, Stevens M, Teuscher U, Thoma RJ, Calhoun VD (2011): A baseline for the multivariate comparison of resting-state networks. *Front Syst Neurosci* 5:2
- Andrews-Hanna JR, Reidler JS, Sepulcre J, Poulin R, Buckner RL (2010): Functional-anatomic fractionation of the brain's default network. *Neuron* 65:550–562.
- Ashburner J (2007): A fast diffeomorphic image registration algorithm. *Neuroimage* 38:95–113.
- Bellec P, Rosa-Neto P, Lyttelton OC, Benali H, Evans AC (2010): Multi-level bootstrap analysis of stable clusters in resting-state fMRI. *Neuroimage* 51:1126–1139.
- Braak H, Braak E (1991): Neuropathological staging of Alzheimer-related changes. *Acta Neuropathol* 82:239–259.
- Brier MR, Thomas JB, Snyder AZ, Benzinger TL, Zhang D, Raichle ME, Holtzman DM, Morris JC, Ances BM (2012): Loss of intranetwork and internetwork resting state functional connections with Alzheimer's disease progression. *J Neurosci* 32:8890–8899.
- Buckner RL, Sepulcre J, Talukdar T, Krienen FM, Liu H, Hedden T, Andrews-Hanna JR, Sperling RA, Johnson KA (2009): Cortical hubs revealed by intrinsic functional connectivity: mapping, assessment of stability, and relation to Alzheimer's disease. *J Neurosci* 29:1860–1873.
- Buckner RL, Snyder AZ, Shannon BJ, LaRossa G, Sachs R, Fotenos AF, Sheline YI, Klunk WE, Mathis CA, Morris JC, Mintun MA (2005): Molecular, structural, and functional characterization of Alzheimer's disease: evidence for a relationship between default activity, amyloid, and memory. *J Neurosci* 25:7709–7717.
- Chetelat G, Desgranges B, Landeau B, Mezenge F, Poline JB, de la Sayette V, Viader F, Eustache F, Baron JC (2008): Direct voxel-based comparison between grey matter hypometabolism and atrophy in Alzheimer's disease. *Brain* 131:60–71.
- Chetelat G, Villain N, Desgranges B, Eustache F, Baron JC (2009): Posterior cingulate hypometabolism in early Alzheimer's disease: what is the contribution of local atrophy versus disconnection? *Brain* 132:e133, author reply e134.
- Cohen AL, Fair DA, Dosenbach NU, Miezin FM, Dierker D, Van Essen DC, Schlaggar BL, Petersen SE (2008): Defining functional areas in individual human brains using resting functional connectivity MRI. *Neuroimage* 41:45–57.
- Crossley NA, Mechelli A, Scott J, Carletti F, Fox PT, McGuire P, Bullmore ET (2014): The hubs of the human connectome are generally implicated in the anatomy of brain disorders. *Brain* 137:2382–2395.
- Damoiseaux JS, Prater KE, Miller BL, Greicius MD (2012): Functional connectivity tracks clinical deterioration in Alzheimer's disease. *Neurobiol Aging* 33:828.e19–e30.
- Damoiseaux JS, Rombouts SA, Barkhof F, Scheltens P, Stam CJ, Smith SM, Beckmann CF (2006): Consistent resting-state networks across healthy subjects. *Proc Natl Acad Sci USA* 103:13848–13853.
- Das SR, Pluta J, Mancuso L, Kliot D, Yushkevich PA, Wolk DA (2015): Anterior and posterior MTL networks in aging and MCI. *Neurobiol Aging* 36:S141–S150, S150 e1.
- Dosenbach NU, Fair DA, Miezin FM, Cohen AL, Wenger KK, Dosenbach RA, Fox MD, Snyder AZ, Vincent JL, Raichle ME, Schlaggar BL, Petersen SE (2007): Distinct brain networks for adaptive and stable task control in humans. *Proc Natl Acad Sci U S A* 104:11073–11078.
- Drzezga A, Becker JA, Van Dijk KR, Sreenivasan A, Talukdar T, Sullivan C, Schultz AP, Sepulcre J, Putcha D, Greve D, Johnson KA, Sperling RA (2011): Neuronal dysfunction and disconnection of cortical hubs in non-demented subjects with elevated amyloid burden. *Brain* 134:1635–1646.
- Edison P, Archer HA, Hinz R, Hammers A, Pavese N, Tai YF, Hotton G, Cutler D, Fox N, Kennedy A, Rossor M, Brooks DJ (2007): Amyloid, hypometabolism, and cognition in Alzheimer disease: an [11C]PIB and [18F]FDG PET study. *Neurology* 68:501–508.
- Fan L, Wang J, Zhang Y, Han W, Yu C, Jiang T (2014): Connectivity-based parcellation of the human temporal pole using diffusion tensor imaging. *Cereb Cortex* 24:3365–3378.
- Fjell AM, Amlie, IK, Sneve, MH, Grydeland, H, Tamnes, CK, Chaplin, TA, Rosa, MG, Walhovd, KB (2014): The roots of Alzheimer's disease: are high-expanding cortical areas preferentially targeted? *Cereb Cortex* 25:2556–2565.
- Fjell AM, McEvoy L, Holland D, Dale AM, Walhovd KB (2013): Brain changes in older adults at very low risk for Alzheimer's disease. *J Neurosci* 33:8237–8242.
- Forster S, Grimmer T, Miederer I, Henriksen G, Yousefi BH, Graner P, Wester HJ, Forstl H, Kurz A, Dickerson BC, Bartenstein P, Drzezga A (2012): Regional expansion of hypometabolism in Alzheimer's disease follows amyloid deposition with temporal delay. *Biol Psychiatry* 71:792–797.
- Fox MD, Corbetta M, Snyder AZ, Vincent JL, Raichle ME (2006): Spontaneous neuronal activity distinguishes human dorsal and ventral attention systems. *Proc Natl Acad Sci USA* 103:10046–10051.
- Fox MD, Snyder AZ, Vincent JL, Corbetta M, Van Essen DC, Raichle ME (2005): The human brain is intrinsically organized into dynamic, anticorrelated functional networks. *Proc Natl Acad Sci USA* 102:9673–9678.
- Glodzik L, Kuceyeski A, Rusinek H, Tsui W, Mosconi L, Li Y, Osorio RS, Williams S, Randall C, Spector N, McHugh P, Murray J, Pirraglia E, Vallabhajosula S, Raj A, de Leon MJ (2014): Reduced glucose uptake and Abeta in brain regions with hyperintensities in connected white matter. *Neuroimage* 100:684–691.
- Gour N, Felician O, Didic M, Koric L, Gueriot C, Chanoine V, Confort-Gouny S, Guye M, Ceccaldi M, Ranjeva JP (2014): Functional connectivity changes differ in early and late-onset Alzheimer's disease. *Hum Brain Mapp* 35:2978–2994.
- Gour N, Ranjeva JP, Ceccaldi M, Confort-Gouny S, Barbeau E, Soulier E, Guye M, Didic M, Felician O (2011): Basal functional connectivity within the anterior temporal network is associated with performance on declarative memory tasks. *Neuroimage* 58:687–697.
- Greicius MD, Krasnow B, Reiss AL, Menon V (2003): Functional connectivity in the resting brain: a network analysis of the default mode hypothesis. *Proc Natl Acad Sci USA* 100:253–258.
- Greicius MD, Srivastava G, Reiss AL, Menon V (2004): Default-mode network activity distinguishes Alzheimer's disease from healthy aging: evidence from functional MRI. *Proc Natl Acad Sci USA* 101:4637–4642.
- Grothe M, Heinsen H, Teipel S (2013): Longitudinal measures of cholinergic forebrain atrophy in the transition from healthy aging to Alzheimer's disease. *Neurobiol Aging* 34:1210–1220.

- Grothe MJ, Ewers M, Krause B, Heinsen H, Teipel SJ (2014): Basal forebrain atrophy and cortical amyloid deposition in nondemented elderly subjects. *Alzheimers Dement* 10:S344–S353.
- Grothe, MJ, Heinsen, H, Amaro, EJ, Grinberg, LT, Teipel, SJ: Cognitive Correlates of Basal Forebrain Atrophy and Associated Cortical Hypometabolism in Mild Cognitive Impairment. *Cereb Cortex*, in press.
- Jagust WJ, Mormino EC (2011): Lifespan brain activity, beta-amyloid, and Alzheimer's disease. *Trends Cogn Sci* 15:520–526.
- Jones DT, Vemuri P, Murphy MC, Gunter JL, Senjem ML, Machulda MM, Przybelski SA, Gregg BE, Kantarci K, Knopman DS, Boeve BF, Petersen RC, Jack CRJ (2012): Non-stationarity in the “resting brain's” modular architecture. *PLoS One* 7:e39731.
- Kahn I, Andrews-Hanna JR, Vincent JL, Snyder AZ, Buckner RL (2008): Distinct cortical anatomy linked to subregions of the medial temporal lobe revealed by intrinsic functional connectivity. *J Neurophysiol* 100:129–139.
- Kljajevic V, Grothe MJ, Ewers M, Teipel S (2014): Distinct pattern of hypometabolism and atrophy in preclinical and predementia Alzheimer's disease. *Neurobiol Aging* 35:1973–1981.
- Koch W, Teipel S, Mueller S, Benninghoff J, Wagner M, Bokde AL, Hampel H, Coates U, Reiser M, Meindl T (2012): Diagnostic power of default mode network resting state fMRI in the detection of Alzheimer's disease. *Neurobiol Aging* 33:466–478.
- La Joie R, Perrotin A, Barre L, Hommet C, Mezenge F, Ibazizene M, Camus V, Abbas A, Landeau B, Guilloteau D, de La Sayette V, Eustache F, Desgranges B, Chetelat G (2012): Region-specific hierarchy between atrophy, hypometabolism, and beta-amyloid (A β) load in Alzheimer's disease dementia. *J Neurosci* 32:16265–16273.
- Landau SM, Breault C, Joshi AD, Pontecorvo M, Mathis CA, Jagust WJ, Mintun MA (2013): Amyloid-beta imaging with Pittsburgh compound B and florbetapir: comparing radio-tracers and quantification methods. *J Nucl Med* 54:70–77.
- Leech R, Braga R, Sharp DJ (2012): Echoes of the brain within the posterior cingulate cortex. *J Neurosci* 32:215–222.
- Lehmann M, Madison CM, Ghosh PM, Seeley WW, Mormino E, Greicius MD, Gorno-Tempini ML, Kramer JH, Miller BL, Jagust WJ, Rabinovici GD (2013): Intrinsic connectivity networks in healthy subjects explain clinical variability in Alzheimer's disease. *Proc Natl Acad Sci USA* 110:11606–11611.
- Mars RB, Sallet J, Schuffelgen U, Jbabdi S, Toni I, Rushworth MF (2012): Connectivity-based subdivisions of the human right “temporoparietal junction area”: evidence for different areas participating in different cortical networks. *Cereb Cortex* 22: 1894–1903.
- McKhann G, Drachman D, Folstein M, Katzman R, Price D, Stadlan EM (1984): Clinical diagnosis of Alzheimer's disease: report of the NINCDS-ADRDA Work Group under the auspices of Department of Health and Human Services Task Force on Alzheimer's Disease. *Neurology* 34:939–944.
- McKhann GM, Knopman DS, Chertkow H, Hyman BT, Jack CRJ, Kawas CH, Klunk WE, Koroshetz WJ, Manly JJ, Mayeux R, Mohs RC, Morris JC, Rossor MN, Scheltens P, Carrillo MC, Thies B, Weintraub S, Phelps CH (2011): The diagnosis of dementia due to Alzheimer's disease: recommendations from the National Institute on Aging-Alzheimer's Association workgroups on diagnostic guidelines for Alzheimer's disease. *Alzheimers Dement* 7:263–269.
- Mevel K, Desgranges B, Baron JC, Landeau B, De la Sayette V, Viader F, Eustache F, Chetelat G (2007): Detecting hippocampal hypometabolism in Mild Cognitive Impairment using automatic voxel-based approaches. *Neuroimage* 37:18–25.
- Mosconi L, Andrews RD, Matthews DC (2013): Comparing brain amyloid deposition, glucose metabolism, and atrophy in mild cognitive impairment with and without a family history of dementia. *J Alzheimers Dis* 35:509–524.
- Myers N, Pasquini L, Gottler J, Grimmer T, Koch K, Ortner M, Neitzel J, Muhlau M, Forster S, Kurz A, Forstl H, Zimmer C, Wohlschlagger AM, Riedl V, Drzezga A, Sorg C (2014): Within-patient correspondence of amyloid-beta and intrinsic network connectivity in Alzheimer's disease. *Brain* 137:2052–2064.
- Oh H, Habeck C, Madison C, Jagust W (2014): Covarying alterations in A β deposition, glucose metabolism, and gray matter volume in cognitively normal elderly. *Hum Brain Mapp* 35: 297–308.
- Pascual B, Masdeu JC, Hollenbeck M, Makris N, Insausti R, Ding SL, Dickerson BC (2015): Large-scale brain networks of the human left temporal pole: a functional connectivity MRI study. *Cereb Cortex* 25:680–702.
- Pasquini L, Scherr M, Tahmasian M, Meng C, Myers NE, Ortner M, Muhlau M, Kurz A, Forstl H, Zimmer C, Grimmer T, Wohlschlagger AM, Riedl V, Sorg C (2015): Link between hippocampus' raised local and eased global intrinsic connectivity in AD. *Alzheimers Dement* 11:475–484.
- Power JD, Cohen AL, Nelson SM, Wig GS, Barnes KA, Church JA, Vogel AC, Laumann TO, Miezin FM, Schlaggar BL, Petersen SE (2011): Functional network organization of the human brain. *Neuron* 72:665–678.
- Price JL (2007): Definition of the orbital cortex in relation to specific connections with limbic and visceral structures and other cortical regions. *Ann N Y Acad Sci* 1121:54–71.
- Ranganath C, Ritzche M (2012): Two cortical systems for memory-guided behaviour. *Nat Rev Neurosci* 13:713–726.
- Royall DR, Palmer RF, Vidoni ED, Honea RA, Burns JM (2012): The default mode network and related right hemisphere structures may be the key substrates of dementia. *J Alzheimers Dis* 32:467–478.
- Sala-Llonch R, Bosch B, Arenaza-Urquijo EM, Rami L, Bargallo N, Junque C, Molinuevo JL, Bartres-Faz D (2010): Greater default-mode network abnormalities compared to high order visual processing systems in amnesic mild cognitive impairment: an integrated multi-modal MRI study. *J Alzheimers Dis* 22:523–539.
- Salami A, Pudas S, Nyberg L (2014): Elevated hippocampal resting-state connectivity underlies deficient neurocognitive function in aging. *Proc Natl Acad Sci USA* 111:17654–17659.
- Seeley WW, Crawford RK, Zhou J, Miller BL, Greicius MD (2009): Neurodegenerative diseases target large-scale human brain networks. *Neuron* 62:42–52.
- Seeley WW, Menon V, Schatzberg AF, Keller J, Glover GH, Kenna H, Reiss AL, Greicius MD (2007): Dissociable intrinsic connectivity networks for salience processing and executive control. *J Neurosci* 27:2349–2356.
- Sepulcre J, Sabuncu MR, Yeo TB, Liu H, Johnson KA (2012): Step-wise connectivity of the modal cortex reveals the multimodal organization of the human brain. *J Neurosci* 32:10649–10661.
- Sheline YI, Raichle ME, Snyder AZ, Morris JC, Head D, Wang S, Mintun MA (2010): Amyloid plaques disrupt resting state default mode network connectivity in cognitively normal elderly. *Biol Psychiatry* 67:584–587.
- Shin J, Lee SY, Kim SJ, Kim SH, Cho SJ, Kim YB (2010): Voxel-based analysis of Alzheimer's disease PET imaging using a

- triplet of radiotracers: PIB, FDDNP, and FDG. *Neuroimage* 52: 488–496.
- Shirer WR, Ryali S, Rykhlevskaia E, Menon V, Greicius MD (2012): Decoding subject-driven cognitive states with whole-brain connectivity patterns. *Cereb Cortex* 22:158–165.
- Smith SM, Fox PT, Miller KL, Glahn DC, Fox PM, Mackay CE, Filippini N, Watkins KE, Toro R, Laird AR, Beckmann CF (2009): Correspondence of the brain's functional architecture during activation and rest. *Proc Natl Acad Sci USA* 106:13040–13045.
- Sorg C, Riedl V, Muhlau M, Calhoun VD, Eichele T, Laer L, Drzezga A, Forstl H, Kurz A, Zimmer C, Wohlschlagel AM (2007): Selective changes of resting-state networks in individuals at risk for Alzheimer's disease. *Proc Natl Acad Sci USA* 104:18760–18765.
- Sperling RA, Aisen PS, Beckett LA, Bennett DA, Craft S, Fagan AM, Iwatsubo T, Jack CRJ, Kaye J, Montine TJ, Park DC, Reiman EM, Rowe CC, Siemers E, Stern Y, Yaffe K, Carrillo MC, Thies B, Morrison-Bogorad M, Wagster MV, Phelps CH (2011): Toward defining the preclinical stages of Alzheimer's disease: recommendations from the National Institute on Aging-Alzheimer's Association workgroups on diagnostic guidelines for Alzheimer's disease. *Alzheimers Dement* 7:280–292.
- Sperling RA, Laviolette PS, O'Keefe K, O'Brien J, Rentz DM, Pihlajamaki M, Marshall G, Hyman BT, Selkoe DJ, Hedden T, Buckner RL, Becker JA, Johnson KA (2009): Amyloid deposition is associated with impaired default network function in older persons without dementia. *Neuron* 63:178–188.
- Spires-Jones TL, Hyman BT (2014): The intersection of amyloid beta and tau at synapses in Alzheimer's disease. *Neuron* 82: 756–771.
- Teipel S, Heinsen H, Amaro EJ, Grinberg LT, Krause B, Grothe M (2014): Cholinergic basal forebrain atrophy predicts amyloid burden in Alzheimer's disease. *Neurobiol Aging*, 35:482–491.
- Tosun D, Schuff N, Mathis CA, Jagust W, Weiner MW (2011): Spatial patterns of brain amyloid-beta burden and atrophy rate associations in mild cognitive impairment. *Brain* 134:1077–1088.
- Vemuri P, Whitwell JL, Kantarci K, Josephs KA, Parisi JE, Shiung MS, Knopman DS, Boeve BF, Petersen RC, Dickson DW, Jack CRJ (2008): Antemortem MRI based STructural Abnormality iNDex (STAND)-scores correlate with postmortem Braak neurofibrillary tangle stage. *Neuroimage* 42:559–67.
- Villeneuve S, Wirth M, La Joie R (2015): Are AD-typical regions the convergence point of multiple pathologies? *Front Aging Neurosci* 7:42
- Vincent JL, Kahn I, Snyder AZ, Raichle ME, Buckner RL (2008): Evidence for a frontoparietal control system revealed by intrinsic functional connectivity. *J Neurophysiol* 100:3328–3342.
- Vincent JL, Snyder AZ, Fox MD, Shannon BJ, Andrews JR, Raichle ME, Buckner RL (2006): Coherent spontaneous activity identifies a hippocampal-parietal memory network. *J Neurophysiol* 96: 3517–3531.
- Whitwell JL, Przybelski SA, Weigand SD, Knopman DS, Boeve BF, Petersen RC, Jack CRJ (2007): 3D maps from multiple MRI illustrate changing atrophy patterns as subjects progress from mild cognitive impairment to Alzheimer's disease. *Brain* 130: 1777–1786.
- Yeo BT, Krienen FM, Sepulcre J, Sabuncu MR, Lashkari D, Hollinshead M, Roffman JL, Smoller JW, Zollei L, Polimeni JR, Fischl B, Liu H, Buckner RL (2011): The organization of the human cerebral cortex estimated by intrinsic functional connectivity. *J Neurophysiol* 106:1125–1165.
- Zhou J, Gennatas ED, Kramer JH, Miller BL, Seeley WW (2012): Predicting regional neurodegeneration from the healthy brain functional connectome. *Neuron* 73:1216–1227.
- Zhou J, Greicius MD, Gennatas ED, Growdon ME, Jang JY, Rabinovici GD, Kramer JH, Weiner M, Miller BL, Seeley WW (2010): Divergent network connectivity changes in behavioural variant frontotemporal dementia and Alzheimer's disease. *Brain* 133:1352–1367.
- Zhu DC, Majumdar S, Korolev IO, Berger KL, Bozoki AC (2013): Alzheimer's disease and amnesic mild cognitive impairment weaken connections within the default-mode network: a multimodal imaging study. *J Alzheimers Dis* 34:969–984.